

# Development and numerical solution of a mechanistic model for corneal tissue ablation with the 193 nm argon fluoride excimer laser

Brian T. Fisher\* and David W. Hahn

College of Engineering, University of Florida, Gainesville, Florida 32611

Received May 8, 2006; revised August 3, 2006; accepted August 30, 2006;  
posted September 1, 2006 (Doc. ID 70671); published January 10, 2007

We detail the development and implementation of a global ablation model that incorporates a dynamically changing tissue absorption coefficient. Detailed spectroscopic measurements rule out plasma-shielding effects during the laser-tissue interaction and thereby support a photochemical mechanism. The model predicts ablation rate behavior that agrees well with a variety of experimental ablation rate data and that substantially deviates from a static Beer-Lambert model. The dynamic model predicts an enhancement in the tissue absorption coefficient of about 25%–50% as compared with the initial, static value. In addition, the model predicts an increase in the tissue ablation rate as corneal hydration increases, which may provide additional insight into variations in refractive surgery outcome. © 2007 Optical Society of America

OCIS codes: 330.4060, 330.7130, 350.3450.

## 1. INTRODUCTION

Despite the success of the 193 nm argon fluoride (ArF) excimer laser in clinical procedures, the exact ablation process and the nature of the laser-tissue interactions are not completely understood. Recent literature reviews summarize the large body of research that has been devoted to understanding the photochemistry of tissue ablation.<sup>1–3</sup> However, a comprehensive, dynamic model of the excimer laser tissue ablation process has not yet been formulated. To date, descriptions of the interaction between excimer laser radiation and corneal tissue are most often formulated in terms of the Beer-Lambert law, as described in the following equation<sup>1–5</sup>:

$$I(x) = I_0 \exp(-\alpha x). \quad (1)$$

In Eq. (1),  $I(x)$  is the radiation intensity after penetrating to depth  $x$  (cm) in the tissue,  $I_0$  is the laser intensity incident on the tissue surface ( $x=0$ ), and  $\alpha$  ( $\text{cm}^{-1}$ ) is the corneal tissue absorption coefficient for 193 nm radiation. Beer-Lambert behavior is applicable when the incident laser intensity is well below the threshold for ablation, conditions for which the absorption coefficient is referred to as the small-signal or static absorption coefficient.

Equation (1) is readily rearranged to provide an equation for the ablation depth in terms of the absorption coefficient and a prescribed ablation threshold.<sup>6</sup> In such a model, often referred to as a blow-off model, the incident laser pulse intensity decays with penetration depth according to the Beer-Lambert law and, subsequently, ablates tissue until the intensity has decayed to the threshold value. Hence the depth required to decay to the threshold intensity defines the ablation depth for a given incident intensity. One may recast Eq. (1) to provide a linear fit of the ablation depth as a function of the natural logarithm of the incident laser intensity divided by the

ablation threshold intensity. Such an equation yields a slope  $m$  (with  $\mu\text{m}$  as the preferred unit) that is equal to the inverse of the absorption coefficient. Previous studies have reported values ranging from as low as  $2400 \text{ cm}^{-1}$  ( $m=4.2 \mu\text{m}$ ) to as high as  $40,000 \text{ cm}^{-1}$  ( $m=0.25 \mu\text{m}$ ) for the static absorption coefficient of corneal tissue, noting that the high value of  $40,000 \text{ cm}^{-1}$  is generally accepted as providing the best fit of the Beer-Lambert law to experimental corneal tissue ablation data.<sup>6–12</sup> In a recent study, the authors reported a value of  $16,000 \text{ cm}^{-1}$  ( $m=0.63 \mu\text{m}$ ) based on direct measurement of the absorption cross sections of peptide bonds and amino acids characteristic of corneal collagen and the overall composition of corneal tissue.<sup>6</sup>

While the formulation of the Beer-Lambert blow-off model is straightforward, it is not possible to match the wide range of published tissue ablation rate data (as presented below) using a single value of the tissue absorption coefficient. Such behavior suggests that the corneal tissue absorption coefficient is a dynamic quantity under excimer laser ablative conditions; hence the static blow-off ablation model must be adjusted.

Other analytical models of excimer laser ablation, both for polymeric materials and for corneal tissue, have been developed.<sup>4,13–16</sup> Pettit and Sauerbrey developed a model that included the effects of chromophore saturation and multiphoton absorption.<sup>4</sup> Sutcliffe and Srinivasan based a model on a process, referred to as ablative photodecomposition, in which a critical density of broken bonds results from an incident photon flux above a certain threshold density (i.e., ablation threshold).<sup>14</sup> Overall, Srinivasan and co-workers detailed the novel concepts of an ablation threshold and of an ablative absorption coefficient that is larger than the preablative (i.e., static) value; however, their work neglected the transient changes in absorption coefficient within layers of material caused by the photo-

decomposition of long-chain molecules and chromophores prior to reaching the ablation threshold.<sup>14,15</sup> Lukyanchuk *et al.* describe a model based on a four-level electronic structure in a polymeric material, with different absorption cross sections for the different levels.<sup>16</sup> However, the best-fit parameters for 193 nm ablation led to unrealistic values, which the authors concluded to be indicative of a significant change in ablation mechanism at the short ArF laser wavelength.

The practical implications of an improved ablation model are clear. Although clinical procedures (e.g., LASIK) are generally regarded as successful, surgical outcomes would benefit from a deeper understanding of the ablation process. Recently, Jimenez and co-workers have recognized that surgical results could be improved by making modifications to current clinical ablation algorithms, including correction factors for corneal asphericity, laser reflection losses at the corneal surface, off-angle incident exposure, laser polarization, and laser beam profile.<sup>17–21</sup> They found that applying these various correction factors during surgical procedures led to better predictions of the outcomes. Jimenez and co-workers also examined deviations from Beer–Lambert behavior during laser ablation.<sup>22</sup> They modified the Beer–Lambert law by introducing a quadratic logarithmic term and determined that this relationship provided a better fit to experimental ablation rate data as compared with the traditional Beer–Lambert law. While the approach is more empirical in nature and the correction factors do not fundamentally address the physics or chemistry of the laser–tissue interactions, the authors’ approach recognizes the inherent limitations of a static absorption model and therefore shares the common goal of improving clinical procedures through a better understanding of the ablation process.

In the current paper, the excimer laser tissue ablation process is examined in the context of its dynamic nature, and what we believe to be a new mechanistic model of excimer laser corneal tissue ablation is developed. This model incorporates corneal collagen and water constituents, makes use of previously measured absorption properties of corneal tissue, and includes a dynamic absorption coefficient that varies both temporally and spatially during the ablation process. The proposed model is not considered conclusive regarding the exact ablation mechanisms, but rather the model is offered as a starting framework to further pursue the dynamic nature of laser–tissue interactions corresponding to important clinical refractive and therapeutic procedures.

## 2. LASER-INDUCED PLASMA CONSIDERATIONS

In concert, the models discussed above provide a starting place for the 193 nm ablation of corneal tissue in the context of the tissue absorption coefficient and the concept of a dynamic (i.e., transient) laser–tissue coupling process. However, one must also consider an alternative mode of laser–tissue interaction that might explain the apparent enhancement in tissue absorption at increasing laser fluence, namely, plasma formation and subsequent plasma shielding (i.e., plasma absorption of the incident laser pulse). It is well known that the interaction of pulsed la-

ser radiation with a material interface will result in a laser-induced plasma or breakdown above a certain threshold intensity value.<sup>23–26</sup> While the range of excimer laser fluence (i.e., incident exposure) utilized for clinical refractive procedures ( $\sim 200$  to  $600$  mJ/cm<sup>2</sup>) is considered below the threshold region for generation of an unequivocal laser-induced plasma in tissue (e.g., of the order of  $10$  J/cm<sup>2</sup> using a nanosecond-pulsed laser<sup>27</sup>), one must consider the possibility of a weak (i.e., near-threshold) plasma forming in which some plasma shielding might account for the departure from low-signal Beer–Lambert behavior and the apparent trend of an enhanced tissue absorption coefficient.

### A. Laser-Induced Plasma Background

The formation of laser-induced plasmas has been widely studied, as they figure prominently in material processing and form the basis for a wide range of analytical chemistry methodologies, such as laser-ablation inductively coupled plasma spectroscopy and laser-induced plasma spectroscopy. The reader is referred to the literature for more complete details regarding laser-induced plasma formation and plasma characteristics.<sup>28</sup>

Once the plasma is initiated, optical emission is spontaneously produced that is spectrally akin to blackbody radiation. In addition, atomic emission may be superimposed on the continuum emission as the excited-state atoms relax while the plasma cools. It is the presence of this characteristic broadband continuum emission and concomitant distinct atomic emission lines that may be used to signify plasma initiation. One goal of the present study is to either confirm or rule out the possibility of laser-induced plasma formation and subsequent plasma shielding as a candidate for the apparent enhancement in tissue absorptivity during excimer laser ablation. Detailed spectroscopic measurements were undertaken to address this issue.

### B. Corneal Tissue Optical Emission Experiments

Emission spectra were recorded during porcine eye ablation experiments. Whole porcine eyes were used, which were removed following sacrifice, stored on ice, and used within 6 h of collection. A schematic of the experimental configuration for these experiments is shown in Fig. 1. The ArF laser was focused directly on the corneal surface using a 100 mm focal-length lens. Two laser pulse energies were investigated, 3.5 and 5.0 mJ/pulse, which correspond to incident average fluence values of 350 and 500 mJ/cm, respectively, based on the measured  $\sim 1$  mm<sup>2</sup> spot size. These fluence values are consistent with the range of clinical fluences associated with excimer laser refractive procedures, with the higher value representing essentially an upper (i.e., limiting) value with regard to clinical relevance.

For all emission measurements, the ArF excimer laser was operated at a repetition rate of 4 Hz to accommodate the computer-controlled spectral data acquisition system. We did not consider repetition rate effects in this study, noting that clinical systems typically operate at less than 100 Hz, while typical laser-induced plasma coupling is limited to time scales of the order of microseconds following plasma initiation.<sup>29</sup> As shown in Fig. 1, optical emis-

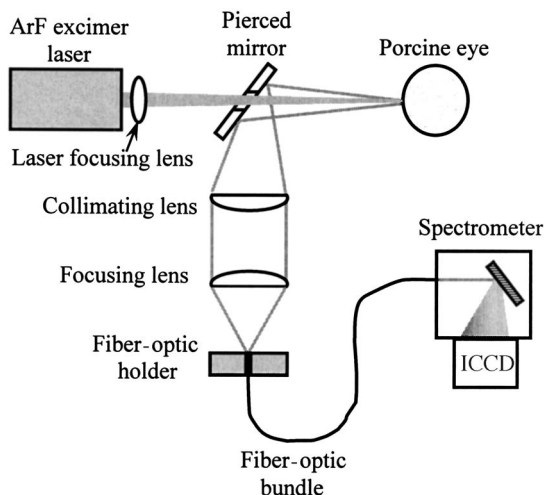


Fig. 1. Schematic of experimental configuration for porcine eye ablation experiments, including laser delivery system and emission collection optics.

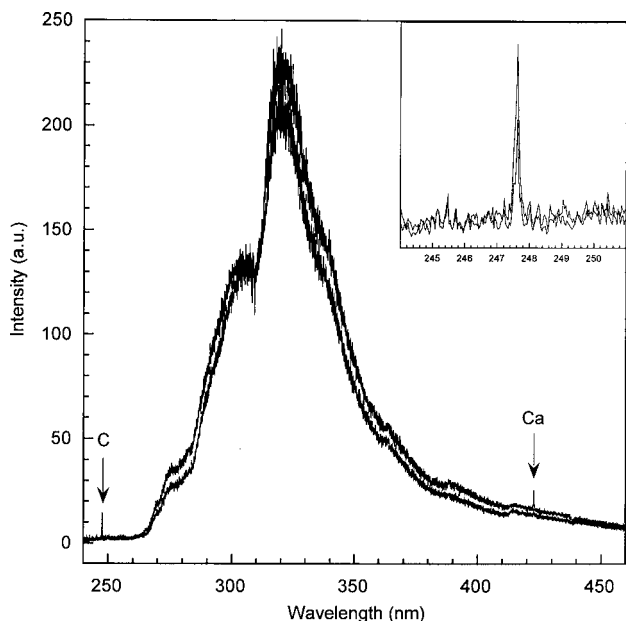


Fig. 2. Emission spectra (corrected for relative intensity) from porcine eyes during ArF excimer laser ablation. The upper and lower spectra correspond to laser energies of 5 and 3.5 mJ/pulse, respectively. The C I and Ca I atomic emission lines are noted at their respective locations, and a closer view of the C I line is shown in the inset.

sion was collected on axis with the incident laser pulse, using a 100 mm square UV-enhanced pierced mirror. The emission was then collimated and lens coupled to a fiber-optic bundle, where it was transmitted to a spectrometer (2400 grooves/mm, 0.2 nm optical resolution) and recorded using an intensified CCD (ICCD). The ICCD gate was appropriately timed to begin immediately before the excimer laser pulse, and the gate width was set to 300 ns, which together ensured that all emission was recorded.

For each ablation site and energy level, spectra were recorded using an ensemble average of 25 consecutive laser pulses, which was repeated in triplicate, before final averaging of all spectra. To achieve both broad spectral

coverage of the optical emission and high spectral resolution, it was necessary to record spectra over various spectral regions. To ensure an accurate measurement of the relative emission intensity over the entire range, all spectral windows were calibrated for relative spectral response using standard lamps of known spectral irradiance.

The resulting porcine emission spectra are presented in Figs. 2 and 3, corresponding to the broad spectral region from 225 to 450 nm and for the spectral region about 590 nm, respectively. With respect to the formation or absence of a laser-induced plasma, three specific observations in these spectra are noted. First, there is a lack of broadband continuum emission that characterizes laser-induced plasma emission. The most prominent feature in Fig. 2 is the broad peak centered at approximately 320 nm, with no appreciable continuous emission recorded below  $\sim 275$  nm nor beyond  $\sim 450$  nm. Accordingly, the relatively limited spectral emission observed in Fig. 2 discounts its source as plasma continuum radiation.

Second, laser-induced plasma emission is characterized by pronounced atomic emission lines, as noted above. Careful examination of the Fig. 2 spectra reveals very weak atomic emission lines corresponding to carbon at 247.86 nm ( $21,648\text{--}61,982\text{ cm}^{-1}$ ) and calcium at 422.67 nm ( $0\text{--}23,652\text{ cm}^{-1}$ ). These lines are relatively weak and would generally not be resolved in a typical broadband, low-resolution spectrum. The inset in Fig. 2 shows a close-up of the carbon emission line. Additional spectral measurements in the region near 656 nm revealed no trace of the  $H_{\alpha}$  atomic emission line at 656.28 nm. The absence of this emission line is significant because it is readily observed in the early stages of laser-induced plasmas in the presence of even modest amounts of water and is in fact widely used for measurement of

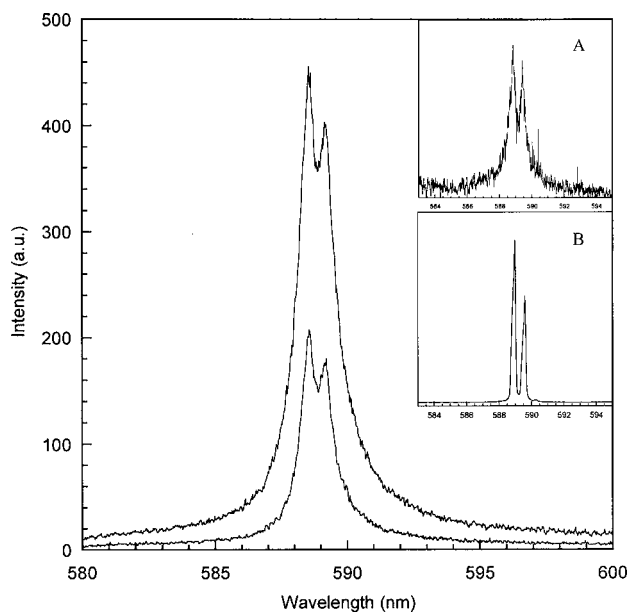


Fig. 3. Porcine eye emission spectra recorded during ablation with laser pulse energies of 3.5 mJ/pulse (lower spectrum) and 5 mJ/pulse (upper spectrum). Inset A is a spectrum corresponding to 193 nm photofragmentation of a NaCl aerosol. Inset B is a spectrum corresponding to Na emission from a 1064 nm laser-induced plasma in a sodium-containing aerosol.

free-electron densities via Stark broadening.<sup>29–31</sup> Finally, the spectral region near 590 nm revealed a weak but measurable emission feature corresponding to the atomic sodium doublet at 589.00 and 589.95 nm. This sodium emission feature is presented in Fig. 3.

While one might be tempted to attribute the C, Ca, and Na atomic emission features to plasma formation, a careful analysis is consistent with the above conclusion pointing to the lack of plasma initiation. UV lasers, notably the 193 nm ArF, have been known to cause dissociation of molecular compounds and to create electronically excited photofragments, which fluoresce as they relax.<sup>32,33</sup> The resulting fluorescence emission lines are often broadened, because the relatively large amount of available photon energy from the UV laser (6.3 eV for ArF) can perturb the energy levels of the fragment species or atoms. Published studies, where emission was recorded following laser photofragmentation of sodium-containing aerosols, have shown Na I emission with characteristics similar to the current porcine eye fluorescence experiments in Fig. 3.<sup>34,35</sup> Such broadened atomic emission line spectra stand in contrast to the narrow atomic emission line profiles typically observed with sodium emission via laser-induced plasma excitation.

To illustrate the above comments, two additional spectra are displayed in the inset of Fig. 3. The upper spectrum (inset A) was recorded directly from the 193 nm photofragmentation of a sodium chloride aerosol using an optical detection system nearly identical to that in the corneal ablation experiments. The similarity between the two spectra is remarkable, including the line broadening and unresolved emission peaks. In contrast, the lower inset spectrum (inset B) corresponds to sodium emission from a true laser-induced plasma formed in a sodium-seeded aerosol stream. The spectrum was recorded with the exact spectrometer-ICCD system used to record the corneal emission spectra; hence there is identical spectral resolution. Note the narrow sodium atomic linewidth observed with the true laser-induced plasma and the essentially baseline-resolved sodium doublet. Clearly, the sodium emission lines recorded with the porcine corneal tissue ablation experiments are consistent with 193 nm photofragmentation, not plasma formation. The carbon and calcium emission lines are similarly attributed to photofragmentation. In particular, note that the calcium emission reported in a true laser-induced plasma spectroscopy study of corneal tissue was primarily attributed to the ionized calcium lines at 393.37 and 396.85 nm, which dominated the neutral calcium emission line at 422.67 nm.<sup>27</sup> As noted above, only the faint 422.67 nm neutral emission line is observed in Fig. 2, while the two calcium-ion lines are completely absent. In view of the above comments, the observed atomic emission spectral features, and lack thereof, are all consistent with the absence of laser-induced plasma formation.

Third, the temporal and pulse energy dependences of the observed ablation emission spectra are not indicative of a typical laser-induced plasma process. To explore the temporal dependence of the optical emission, additional measurements were recorded by adding an extra 100 ns of delay to the detector gate. With this relatively short additional delay, no optical emission was observed. In con-

trast, laser-induced plasmas display pronounced emission for time scales approaching microseconds to tens of microseconds when created with a nanosecond-scale laser pulse, as used in the present study. Furthermore, laser-induced plasma emission generally scales strongly with laser pulse energy, notably so at near-threshold values. However, note that the two spectra in Fig. 2, corresponding to a marked difference in laser fluence, are nearly indistinguishable with regard to spectral intensity. Such behavior is not consistent with laser-induced plasma formation.

Considering the above observations and comments in aggregate, we conclude that the spectral data in Fig. 2 represent direct fluorescence from the rich organic matrix of corneal tissue. Fluorescence is a prompt phenomenon (lifetimes of the order of  $10^{-9}$  to  $10^{-7}$  s), as is the case in the current study. Furthermore, the broad feature shown in Fig. 2 is typical of the fluorescence observed for biological materials, which usually display spectrally broad but clearly defined bands.<sup>36</sup> It is proposed that there are two fluorescence-related processes that result from the current corneal ablation experiments. Specifically, the broadband emission, including both the low-intensity continuum and the broad peak centered at 320 nm, is a result of prompt fluorescence from tissue surrounding the ablation zone (i.e., below and adjacent to). This tissue absorbs a portion of the 193 nm excimer laser light that is not sufficient to cause ablation (i.e., below the ablation threshold); hence the tissue remains intact to fluoresce. If one considers the blow-off model of laser penetration, then the intact fluorescing tissue is exposed to an essentially constant fluence regardless of the incident value, and therefore the fluorescence signal is nominally independent of the incident laser fluence, as observed in Fig. 2. Superimposed on the broadband emission are discrete atomic emission lines that we conclude result from photofragmentation fluorescence. This process occurs within the ablated mass and is therefore dependent on the incident laser fluence. Overall, this explains why the atomic emission lines appear to scale somewhat proportionately with laser energy, whereas the broadband emission does not. In view of the detailed spectroscopic analysis of the corneal ablation process under clinically relevant fluences, the concept of plasma formation and plasma shielding of the incident laser pulse can be discounted.

### 3. DYNAMIC ABLATION MODEL

The authors have previously reported that the corneal tissue absorption coefficient (small-signal value) is  $16,000\text{ cm}^{-1}$  for 193 nm radiation, based on direct measurements of collagen and water absorption cross sections.<sup>6</sup> Furthermore, it was shown that the Beer-Lambert blow-off model, in conjunction with the measured absorption coefficient, is reasonably accurate in predicting ablation rates of dry collagen films over a moderate range of laser fluence.<sup>6</sup> However, the failure of the Beer-Lambert model to adequately predict a wide range of corneal tissue ablation rates suggests that photochemical effects are induced within the more complex corneal tissue matrix during laser-tissue interaction, resulting in a dynamic perturbation of the tissue optical properties,

namely, the absorption coefficient. Previous research has documented a transient decrease in tissue and collagen transmission (i.e., enhanced absorption) during ArF laser ablation, while time-resolved reflectivity measurements have also demonstrated transient changes in tissue optical properties.<sup>37–42</sup> In concert, such data support the concept of an enhanced absorption coefficient, with respect to the small-signal static value, during ArF laser ablation. In fact, an absorption coefficient of  $40,000\text{ cm}^{-1}$  ( $m = 0.25\text{ }\mu\text{m}$ ), as extracted from a best-fit static Beer–Lambert model, is clearly too high in view of recent measurements.<sup>6</sup> Accordingly, such a large absorption coefficient is considered to reflect the need for considerable enhancement of the small-signal value to fit the experimental data and thereby attempts to capture the dynamic nature of tissue properties during ablation in an adjusted, but nonetheless static, value. The current model, which is based on the Beer–Lambert blow-off model, was developed to further explore the dynamic nature of laser–tissue interactions in the context of observed corneal ablation rate data and current clinical needs.

#### A. Assumptions and Basis of the Ablation Model

The current tissue ablation model is developed by considering four species of interest: (1) collagen, which is divided into amino acid units (i.e., amino acid plus peptide bond); (2) water; (3) a transient absorber (strongly absorbs 193 nm laser light) formed by the interaction of collagen amino acid units with excimer laser photons; and (4) a stable nonabsorber, formed by the interaction of transient absorber (species 3) with surrounding water. The four-species model is considered a global model that represents the ablation mechanics as a whole rather than the fine details of the photochemistry, chemical kinetics, and individual reactions that might take place. This is a common method for modeling complex chemical processes that may involve many reactions and intermediate species. For example, combustion processes are commonly modeled in this way, where the global mechanism may be a single reaction of a combustion fuel and an oxidizer to directly form carbon dioxide and water, while the actual mechanism may involve hundreds of elementary reactions and more than 50 species. In the current dynamic ablation model, the transient absorbing species (species 3) is assigned an absorption cross section that represents the average of all such species.

The current model is considered one-dimensional (1-D) in space such that all spatially dependent quantities are allowed to vary only with depth (i.e.,  $x$  direction) into the tissue. The incident laser pulse temporal waveform is well defined by a Gaussian probability distribution function. In practice, modern clinical refractive laser systems may incorporate flying-spot lasers with Gaussian spatial beam profiles. The surgical implications of Gaussian and uniform beam profiles were examined by Jimenez and co-workers in a recent study.<sup>21</sup> Multidimensional mass, energy, and photon transport were not within the scope of the current study. However, note that a spatial Gaussian laser profile is readily handled with the current 1-D model by simply discretizing the beam profile and run-

ning the 1-D model at each spatial location. Such an approach adds only computational time to the proposed ablation model.

There are several variables and quantities incorporated in the dynamic ablation model that must be reviewed to understand the model itself. All of the important parameters are listed in Table 1. As previously reported, the absorption cross section of the amino acid unit in collagen (species 1),  $\sigma_1$ , is equal to  $1.19 \times 10^{-17}\text{ cm}^2$ , and the absorption cross section of water (species 2),  $\sigma_2$ , is equal to  $4.5 \times 10^{-23}\text{ cm}^2$ .<sup>6</sup> The average absorption cross section of the transient absorbing species, namely,  $\sigma_3$ , is assumed to be larger than  $\sigma_1$  ( $\sigma_3 > \sigma_1$ ) to dynamically enhance the corneal tissue absorption coefficient. The average absorption cross section,  $\sigma_4$ , of the stable, nonabsorbing species (species 4) is much less than  $\sigma_3$  ( $\sigma_4 \ll \sigma_3$ ). The absorption coefficient of corneal tissue is the product of the number density and the absorption cross section of each of these four species at any point in space and time. Therefore, the corneal tissue absorption coefficient, in general, can be described by Eq. (2):

$$\alpha(x, t) = \rho_1(x, t)\sigma_1 + \rho_2(x, t)\sigma_2 + \rho_3(x, t)\sigma_3 + \rho_4(x, t)\sigma_4. \quad (2)$$

Scaling considerations can be used to argue that the second and fourth terms of Eq. (2) are negligible compared with the others, based on the above comments. The absorption cross section of water ( $\sigma_2$ ) is 6 orders of magnitude lower than that of the amino acid unit in collagen ( $\sigma_1$ ), while their respective number densities differ by no more than 1 or 2 orders of magnitude. The third term ( $\rho_3\sigma_3$ ) is considered important because, although the concentration of species 3 is expected to be small, the absorption coefficient is assumed sufficiently large to make this term relevant and, in fact, primarily responsible for the transient enhancement in tissue absorption during ablation. Both the number density and the absorption cross

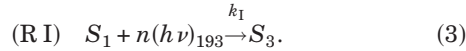
**Table 1. Dynamic Corneal Tissue Ablation Model Parameters**

Description	Symbol	Units
Excimer laser photon flux (at location $x$ and time $t$ )	$I(x, t)$	$\text{cm}^{-2}\text{ s}^{-1}$
Excimer laser fluence	$F$	$\text{mJ}/\text{cm}^2$
Probability distribution function of laser energy	$p(t)$	$\text{s}^{-1}$
Species $i$ , used to represent a particular species in a reaction expression	$S_i$	—
Number density of species $i$ (at $x$ and $t$ )	$\rho_i(x, t)$	$\text{cm}^{-3}$
Number density of 193 nm photons (at $x$ and $t$ )	$\rho_{h\nu}(x, t)$	$\text{cm}^{-3}$
Absorption cross section of species $i$	$\sigma_i$	$\text{cm}^2$
Absorption coefficient of corneal tissue (at $x$ and $t$ )	$\alpha(x, t)$	$\text{cm}^{-1}$
Corneal tissue water fraction (by mass)	$P$	Dimensionless (ranges $0 \rightarrow 1$ )

section of species 4 are expected to be much less than those for the amino acid unit and for water, making their product negligible.

### B. Governing Equations

The global mechanism of the dynamic ablation model is based on two primary reactions. The first is the interaction of the excimer laser photon with the amino acid unit in collagen (species 1), which is labeled reaction I and is described by expression (3):



In this relation, the  $n(h\nu)_{193}$  term represents the absorption of  $n$  excimer laser photons by the amino acid unit. Note that, although reaction I does not explicitly involve water, the implicit assumption of the proposed global dynamic absorption model is the interaction of transient species with water and collagen, including the possibility of multiple reaction steps and pathways. Without water present in the initial tissue matrix, the situation would reduce to the case of dry collagen, for which the static blow-off model has been shown to be a reasonable predictor of ablation.<sup>6</sup> Therefore, water must be present for the global mechanism to proceed. The rate expression for reaction I is given by Eq. (4):

$$\frac{\partial \rho_1(x,t)}{\partial t} = -\rho_1(x,t)\rho_{h\nu}(x,t)^n k_I. \quad (4)$$

The second reaction considered is the interaction between the transient absorbing species (species 3) and water to produce a stable product (species 4). This reaction, labeled reaction II, is shown in expression (5), and the rate expression is shown in Eq. (6):



$$\frac{\partial \rho_2(x,t)}{\partial t} = -\frac{\partial \rho_4(x,t)}{\partial t} = -\rho_2(x,t)\rho_3(x,t)k_{II}. \quad (6)$$

Because species 3 appears in both reactions I and II [expressions (3) and (5)], its rate of change can be expressed by Eq. (7):

$$\frac{\partial \rho_3(x,t)}{\partial t} = \rho_1(x,t)\rho_{h\nu}(x,t)^n k_I - \rho_2(x,t)\rho_3(x,t)k_{II}. \quad (7)$$

To complete the formulation, the Beer–Lambert law is used to describe the relationship between the photon density and the penetration depth into the tissue. The differential form of the Beer–Lambert law is shown in Eq. (8):

$$dI = -(\alpha I)dx. \quad (8)$$

However, the photon flux  $I(x,t)$  is directly related to the photon density  $\rho_{h\nu}$ . Therefore, the Beer–Lambert law can be rewritten as shown in Eq. (9), noting that  $\alpha$  is the corneal tissue absorption coefficient described in Eq. (2),

$$\frac{\partial \rho_{h\nu}(x,t)}{\partial x} = -\alpha \rho_{h\nu}(x,t). \quad (9)$$

The final differential form of the Beer–Lambert law used in the dynamic ablation model is shown in Eq. (10), where  $\alpha$  is now a function of space and time as defined by the relevant species concentrations and their respective cross sections:

$$\begin{aligned} \frac{\partial \rho_{h\nu}(x,t)}{\partial x} = & -[\rho_1(x,t)\sigma_1 + \rho_2(x,t)\sigma_2 + \rho_3(x,t)\sigma_3 \\ & + \rho_4(x,t)\sigma_4]\rho_{h\nu}(x,t). \end{aligned} \quad (10)$$

As discussed above, prior research suggests that there is a physical phenomenon associated with the tissue ablation process; namely, when the photon density reaches the ablation threshold, ensuing photofragmentation results in a volume expansion of the affected tissue, by which the subsequent internal stress ultimately drives out the bulk material.<sup>14,15,43</sup> The exact degree of ablative tissue expansion is not known; hence a modest expansion of 10% was used in the current dynamic ablation model.

### C. Solution Method

As shown above, there are four partial differential equations, represented by Eqs. (4), (6), (7), and (10), that form the basis of the model. The equations were solved simultaneously using the Euler forward method, a relatively simple forward finite-difference solution method. There were several issues to consider when choosing the spatial and temporal step sizes, including the ablation rate resolution, computational error, numerical stability, and computational speed. It was desired to have ablation rate results with appropriate resolution to compare with existing experimental data. Nearly all of the available experimental ablation rate data fall below  $1 \mu\text{m}/\text{pulse}$ ; hence submicrometer spatial resolution is necessary. The forward Euler method is a first-order explicit numerical method, which means that the numerical error is related to the square of the step size. Therefore, a small step size is required to minimize computational error and to keep the solution stable. At the same time, a small step size results in a longer computation time; hence it was necessary to find a suitable compromise between these issues.

Based on the physics of the problem, the temporal step size and the spatial step size were linked together by the speed of light in corneal tissue. Once the space step size ( $\Delta x$ ) was chosen, the time step size ( $\Delta t$ ) was calculated by dividing  $\Delta x$  by the speed of light (adjusted by the refractive index of corneal tissue). This linking of spatial and temporal scales also is convenient because, at any given time step, the tissue beyond the current penetration depth is unaffected, and therefore the initial conditions still hold. The final choice of step size for both time and space is discussed in Subsection 3.F.

The numerical computations were implemented in FORTRAN with the initial and boundary conditions detailed below. The program steps through the calculations for a single incident laser pulse and provides output that includes the peak photon density ( $\rho_{h\nu}$ ) and the maximum tissue absorption coefficient ( $\alpha$ ) achieved at each depth

into the corneal tissue. It is assumed that each laser pulse is an isolated event and that there are no interactions or cumulative effects between laser pulses. The ablation depth, which for each single laser pulse is equivalent to the ablation rate, is determined as the depth at which the peak  $\rho_{h\nu}$  decreases to the ablation threshold. The threshold value is the peak  $\rho_{h\nu}$  (i.e., the peak of the Gaussian temporal laser pulse profile) corresponding to the threshold laser fluence of  $50 \text{ mJ/cm}^2$ . This threshold yields a peak photon flux value of approximately  $2.12 \times 10^{14} \text{ cm}^{-3}$  as the critical value. A  $50 \text{ mJ/cm}^2$  ablation threshold for corneal tissue is consistent with the range of experimental data shown in Fig. 9 (below).

The ablation-induced volume expansion was implemented as a 10% reduction in the densities of all four species ( $S_1, S_2, S_3$ , and  $S_4$ ). The program was written such that a one-time density reduction occurs in a single time step at a given tissue depth once the photon density reaches the ablation threshold. The model did not include a 10% reduction in the photon density because the photons continue to propagate through the tissue beyond where the volume expansion occurs. As written, the ablation event proceeds from the surface inward, which is consistent with physical insight as reviewed in the introductory comments.

#### D. Initial and Boundary Conditions

Considering Eqs. (4), (6), (7), and (10), there are five quantities of interest that vary with both space and time—the number densities of the four species in the corneal tissue and the photon number density. Solution of these differential equations requires initial and/or boundary conditions for these quantities. The simplest conditions are imposed on species 3 and 4, which are formed during the laser interaction. By definition, these species have initial number densities equal to zero. These conditions are represented mathematically in Eqs. (11) and (12):

$$\rho_3(x, t = 0) = \rho_{30} = 0, \quad (11)$$

$$\rho_4(x, t = 0) = \rho_{40} = 0. \quad (12)$$

The initial number density of amino acid units (species 1) depends on the corneal mass composition, which is specified as a binary mixture of water and collagen. To investigate the effects of corneal hydration on the ablation rate, the water mass fraction is left as a variable ( $P$ ) that is equal to 0.80 for the base case. This reflects a normal corneal composition of 80% water and 20% collagen. Considering the structure of collagen, it can be calculated that there are  $6.77 \times 10^{21}$  peptide bonds (i.e., amino acid units) per gram of collagen.<sup>6</sup> Furthermore, corneal tissue is assumed to have a mass density of  $1 \text{ g/cm}^3$ , which is consistent with its primary composition of water. Therefore, the initial number density of the amino acid unit can be determined using Eq. (13):

$$\rho_1(x, t = 0) = \rho_{10} = (1 - P)(1 \text{ g/cm}^3)(6.77 \times 10^{21} \text{ g}^{-1}). \quad (13)$$

The initial number density of water molecules also depends on the water mass fraction. Using the Avogadro constant and the molecular weight of water, it can be de-

termined that there are  $3.34 \times 10^{22}$  molecules of water/g of corneal tissue. Again assuming a corneal tissue mass density of  $1 \text{ g/cm}^3$ , the initial number density of water molecules (species 2) can be determined using Eq. (14):

$$\rho_2(x, t = 0) = \rho_{20} = P(1 \text{ g/cm}^3)(3.34 \times 10^{22} \text{ g}^{-1}). \quad (14)$$

It was stated in the formulation of the model that the incident laser energy temporal waveform is assumed to take the form of a Gaussian distribution, as described by Eq. (15):

$$p(t) = \frac{1}{s_{dev} \sqrt{2\pi}} \exp \left[ \frac{-(t - t_{avg})^2}{2s_{dev}^2} \right]. \quad (15)$$

In this distribution function,  $t_{avg}$  is the mean, and  $S_{dev}$  is the standard deviation. These quantities are determined by known parameters of the laser pulse and its time profile. First, it must be recognized that a Gaussian distribution exists over an infinite domain (both positive and negative), while the true laser pulse has a finite existence. However, nearly 100% of the information for a Gaussian distribution is contained within  $t_{avg} \pm 3s_{dev}$ . Therefore, the condition shown in Eq. (16) was imposed:

$$p(t_{avg} \pm 3s_{dev}) = 0. \quad (16)$$

Furthermore, the excimer laser pulse has a full width of approximately 25 ns and a full width at half-maximum value (FWHM) of approximately 10 ns. Conveniently, assigning values of 12.6 and 4.2 ns for  $t_{avg}$  and  $s_{dev}$ , respectively, gives a FWHM of 9.89 ns and satisfies Eq. (15) as well as the condition that the laser pulse ends at approximately 25 ns.

The photon flux at the surface of the cornea is directly related to the laser fluence. Assuming the normal distribution already discussed, a laser fluence  $F$  ( $\text{mJ/cm}^2$ ), and a photon energy equal to the product of Planck's constant ( $h = 6.626 \times 10^{-34} \text{ J s}$ ) and the radiation frequency ( $\nu$ ), the relationship between photon flux ( $\text{photons/cm}^2$ ) and laser fluence is shown in Eq. (17):

$$I(x = 0, t) = F \left( \frac{1}{h\nu} \right) p(t). \quad (17)$$

Photon number density is related to photon flux using the speed of light in corneal tissue ( $c_{cornea}$ ), since the photons propagate through the corneal tissue at this speed. Therefore, the photon number density at the corneal surface can be expressed by Eq. (18):

$$\rho_{h\nu}(x = 0, t) = \frac{I(x = 0, t)}{c_{cor}} = \left( \frac{n_{cor}}{c_{vac}} \right) \left[ F \left( \frac{1}{h\nu} \right) p(t) \right]. \quad (18)$$

A value of 1.376 is used for the refractive index of corneal tissue ( $n_{cornea}$ ). This value is very close to the refractive index of water and is consistent with values reported in the literature for corneal tissue.<sup>44</sup> The photon number density at the corneal surface (i.e., boundary condition) can be expressed in its entirety by the expression shown in Eq. (19), where time is in the units of nanoseconds:

$$\rho_{h\nu}(x=0,t) = \left(\frac{F}{h\nu}\right) \left(\frac{n_{cor}}{c_{vac}}\right) \times \left[\frac{1}{(4.2 \text{ ns})\sqrt{2\pi}}\right] \exp\left[\frac{-(t - 12.6 \text{ ns})^2}{2(4.2 \text{ ns})^2}\right]. \tag{19}$$

**E. Reaction Rate Constants**

The reaction rate constants,  $k_I$  and  $k_{II}$ , are critical parameters that must first be estimated in order to implement the ablation model. First-order estimates of these constants can be obtained using the initial values of the species number densities  $\rho_1$ ,  $\rho_2$ ,  $\rho_3$ , and  $\rho_4$  under typical conditions and a relevant value of the photon density  $\rho_{h\nu}$ . Assuming a typical corneal constituency of 20% collagen and 80% water and using Eqs. (13) and (14), the species number densities  $\rho_1$  and  $\rho_2$  can be estimated as  $1.4 \times 10^{21} \text{ cm}^{-3}$  and  $2.7 \times 10^{22} \text{ cm}^{-3}$ , respectively. As discussed above, the initial values of both  $\rho_3$  and  $\rho_4$  are zero. Assuming a representative clinical laser fluence of  $350 \text{ mJ/cm}^2$  and a corneal tissue refractiveindex of 1.376, and using the peak value of the laser pulse distribution function (i.e.,  $t=12.6 \text{ ns}$ ), Eq. (19) can be used to estimate a peak photon density of  $1.5 \times 10^{15} \text{ cm}^{-3}$ . Note that  $\rho_{h\nu}$  is orders of magnitude lower than  $\rho_1$  and  $\rho_2$ , according to these estimates, which makes  $\rho_{h\nu}$  negligible when the reaction time constants, are estimated, as related below.

The time rate of change in the number density of water molecules (species 2) is dependent on  $\rho_2$  and  $\rho_3$  [see Eq. (6)]. However,  $\rho_3$  is initially zero and will likely remain much smaller than  $\rho_2$  throughout the ablation process. Therefore, Eq. (20) represents a first-order estimate of the time constant for reaction II [expression (5)]<sup>45</sup>:

$$\tau_{II} = \frac{1}{\rho_2 k_{II}}. \tag{20}$$

Using similar logic for reaction I [expression (3)], where  $\rho_1$  is much larger than  $\rho_{h\nu}$ , and assuming that the order of the reaction is unity (i.e.,  $n=1$ ), a first-order estimate of the time constant for reaction I is given by Eq. (21)<sup>45</sup>:

$$\tau_I = \frac{1}{\rho_1 k_I}. \tag{21}$$

Assuming that  $n$  is unity is equivalent to assuming that the photochemical reaction is a single-photon absorption process. This makes subsequent calculations and estimates much more convenient and is considered a valid assumption, given the high photon energy ( $\sim 6.3 \text{ eV}$ ) of 193 nm radiation. Hence the model was implemented for unity  $n$ . All that remains to determine first-order estimates of  $k_I$  and  $k_{II}$  is to estimate the relevant time scales of reactions I and II. Reaction I is considered a prompt process that certainly must occur well within the course of the laser pulse for a dynamic model. Accordingly, because the time scale of reaction I kinetics must be much faster than the nanosecond time scale of the laser pulse,  $\tau_I$  was estimated to be of the order of 10 ps. This is consistent with the dynamics of elementary chemical reactions, which occur on a femtosecond-to-picosecond time

scale.<sup>46</sup> Furthermore, time-resolved transmission measurements (40 ps probe pulse at 220 nm) of hydrated collagen films revealed transient enhancements in absorption over the course of the 10 ns excimer pulse.<sup>41</sup> Reaction II, on the other hand, is considered a slow process that very likely lags behind the laser pulse; hence  $\tau_{II}$  was estimated to be of the order of 1  $\mu\text{s}$ . Such a time scale is consistent with research that probed transient changes in transmission (213 nm) of hydrated collagen films during 193 nm ablation, which revealed a relaxation time of the order of microseconds.<sup>41</sup> These values, which themselves are *ab initio* estimates, determine the first-order estimates of the reaction rate constants as shown in expressions (22) and (23):

$$k_I = \frac{1}{\rho_1 \tau_I} = \frac{1}{(1.4 \times 10^{21} \text{ cm}^{-3})(10 \times 10^{-12} \text{ s})} \approx 7.1 \times 10^{-11} \text{ cm}^3/\text{s}, \tag{22}$$

$$k_{II} = \frac{1}{\rho_2 \tau_{II}} = \frac{1}{(2.7 \times 10^{22} \text{ cm}^{-3})(1 \times 10^{-6} \text{ s})} \approx 3.7 \times 10^{-17} \text{ cm}^3/\text{s}. \tag{23}$$

**F. Results and Discussion**

To validate the numerical and computational methods used in this model, it was first tested against a static Beer–Lambert law. The absorption cross sections of the transient absorber and the stable nonabsorber were set equal to that of collagen (i.e.,  $\sigma_3 = \sigma_4 = \sigma_1 = 1.19 \times 10^{-17} \text{ cm}^2$ ), and the volume expansion under ablative conditions was suppressed, which together effectively removed the dynamic component of the model. Note, however, that the convergence to Beer–Lambert behavior is not exact, in that reaction 2 provides for a slow replacement of water with collagen. Nonetheless, under these conditions, the model was expected to approach Beer–Lambert behavior if the numerical implementation was correct. These conditions were then used to test different step sizes for computational convergence and accuracy. In consideration of these issues, a spatial step size ( $\Delta x$ ) of 20 nm (0.020  $\mu\text{m}$ ) was determined as optimal.

Plots of ablation rate versus laser fluence for both the static Beer–Lambert law and the results from the relaxed dynamic model with  $\sigma_3$  and  $\sigma_4$  set equal to  $\sigma_1$  are shown in Fig. 4. Two important observations from these plots are noted. First, the computational schemes are validated by the observed trend corresponding to near-Beer–Lambert behavior, as expected for these conditions. Second, the overall accuracy is satisfactory using the chosen step size of 20 nm. Over the range of laser fluence, the numerical ablation rates are about 2% lower than the static Beer–Lambert law, which is consistent with the slight increase in absorption due to the effects of reaction 2, as noted above. For all remaining calculations, a spatial step size of 20 nm was used, which corresponds to an associated temporal step size of approximately  $9.2 \times 10^{-8} \text{ ns}$ . Because of this extremely small step size relative to the temporal profile of the laser pulse, numerical error was not a fur-

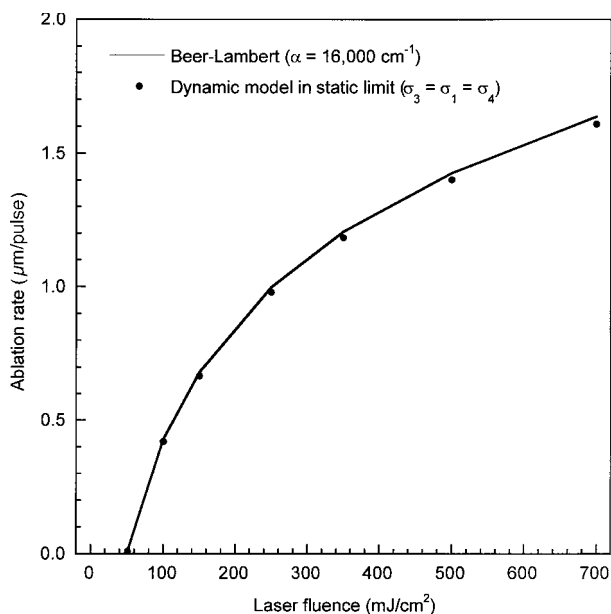


Fig. 4. Comparison of ablation rates predicted by (1) the dynamic ablation model in the static limit, whereby species 3 and 4 have the same absorption cross sections as species 1, and (2) rates predicted by the static Beer-Lambert law. Dynamic model parameters:  $\Delta x = 20$  nm,  $P = 0.8$ ,  $\sigma_3 = \sigma_4 = \sigma_1 = 1.19 \times 10^{-17}$  cm<sup>2</sup>.

ther concern. Under these conditions, a typical program required approximately 1–2 h of run time on a  $\sim 1$  GHz desktop personal computer.

With *ab initio* calculations as a basis and with the results of a simple optimization study (see comments below), a base set of conditions was chosen for the dynamic model. In the base case,  $P = 0.8$  (i.e., 80% water in corneal tissue) and  $\sigma_3 = 4.5 \times 10^{-15}$  cm<sup>2</sup> are used; note that the latter cross section is about 380 times larger than  $\sigma_1$  (i.e., amino acid-peptide bond cross section). With the slower kinetics associated with reaction II, the *ab initio* calculation ( $k_{II} = 3.7 \times 10^{-17}$  cm<sup>3</sup>/s) was retained. However, the reaction I rate constant was increased by a factor of 10, yielding a final value of  $k_I = 7.1 \times 10^{-10}$  cm<sup>3</sup>/s, which remains consistent with the expected kinetic time scales.

Although *ab initio* calculations were made to determine physically realistic estimates of the model parameters, as related above, a brief parametric study was also performed to determine the effect of varying these relevant values (i.e.,  $\sigma_3$ ,  $\sigma_4$ ,  $k_I$ , and  $k_{II}$ ). An example of such calculations is presented in Fig. 5, which shows the decay of the peak photon density as a function of tissue depth for the base case along with several perturbations. As might be expected, increasing the rate of reaction I results in a marked increase in the rate of dynamic enhancement in absorption, thereby yielding a much more rapid decay profile. Conversely, reducing the kinetic rate of reaction I results in a less severe decay profile, which converges to Beer-Lambert behavior as  $k_I$  is significantly reduced. Altering the cross section of species 3 ( $\sigma_3$ ) has the effect of shifting the curves up or down while generally maintaining the overall decay profile. The base case as defined above was used for all subsequent calculations.

At a laser fluence of 350 mJ/cm<sup>2</sup>, which is consistent with clinical refractive procedures, the decay of the peak photon density was calculated as a function of laser radia-

tion penetration into the corneal tissue. Figure 6 shows a plot of the peak photon density ( $\rho_{h\nu}$ ) as a function of tissue depth, where the peak density is the maximum value predicted at each depth over the time course of the laser pulse (i.e., the peak of the temporal beam profile). The ablation threshold is shown as a horizontal line corresponding to a peak photon density of  $2.12 \times 10^{-14}$  cm<sup>-3</sup>, and the predicted ablation depths both from the dynamic model and from the two relevant cases of the Beer-Lambert law are indicated. The profile predicted by the dynamic model is an enhanced exponential decay that deviates significantly from static Beer-Lambert behavior. At very shallow locations, the dynamic model profile is similar to the static exponential decay predicted by the Beer-Lambert law with an absorption coefficient of 40,000 cm<sup>-1</sup>. With increasing depth, the dynamic model decay gradually shifts toward the exponential decay predicted by the 16,000 cm<sup>-1</sup> case of the Beer-Lambert law. This gradual shift gives the dynamic model a profile that is clearly different from a static exponential decay, which is consistent with the motivating factors of this study.

The behavior predicted by the dynamic model is further illustrated by temporal profiles of the photon density and the tissue absorption coefficient. Figure 7 shows photon density profiles as a function of time at five tissue depths, with the temporal photon density profile of the incident laser pulse (350 mJ/cm<sup>2</sup>) included as a reference. Owing to the large number of time steps necessary to simulate the entire 25 ns laser pulse, it was impractical to sample data at every point in time. For simplicity, only 1000 points were sampled to assemble each time profile, which provides an adequate temporal resolution. The first observation regarding Fig. 7 is that the overall magnitude of the photon density decreases with increasing tissue

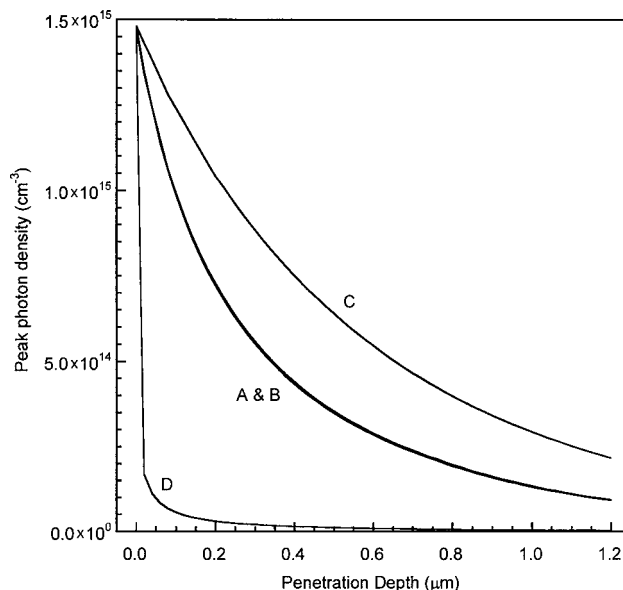


Fig. 5. Parametric study showing the peak photon density as a function of tissue depth as predicted by the dynamic ablation model for an incident laser fluence of 350 mJ/cm<sup>2</sup>. Curve A is the base case using the following parameters:  $k_I = 7.1 \times 10^{-10}$  cm<sup>3</sup>/s,  $k_{II} = 3.7 \times 10^{-17}$  cm<sup>3</sup>/s,  $\sigma_3 = 4.5 \times 10^{-15}$  cm<sup>2</sup>, and  $\sigma_4 = 4.5 \times 10^{-24}$  cm<sup>2</sup>. Curve B reflects a 20% decrease in  $k_I$  and a 20% increase in  $\sigma_3$ ; curve C reflects a tenfold decrease in  $k_I$ ; and curve D reflects a 100-fold increase in  $k_I$  and a tenfold increase in  $\sigma_3$ .

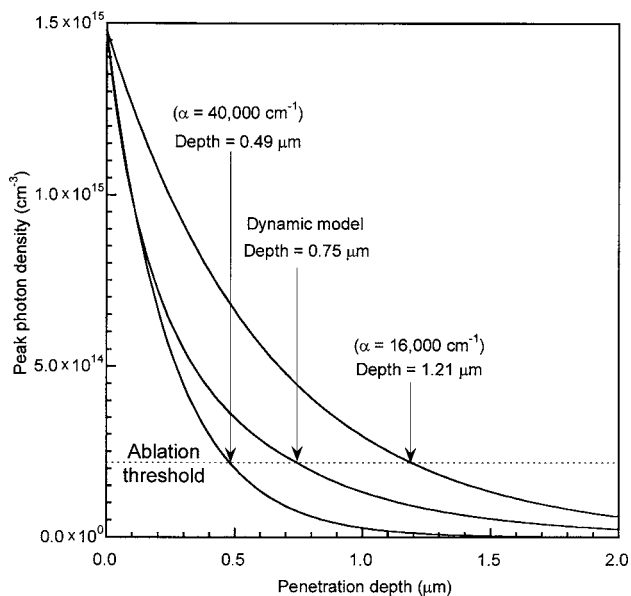


Fig. 6. Comparison of peak photon density as a function of tissue depth as predicted by the dynamic ablation model and by the static Beer-Lambert blow-off model for absorption coefficients of 16,000 and 40,000  $\text{cm}^{-1}$ . A dashed horizontal line indicates the ablation threshold, and the ablation depths predicted by the models are shown. Dynamic model parameters:  $\Delta x=20 \text{ nm}$ ,  $P=0.8$ ,  $\sigma_3=4.5 \times 10^{-15} \text{ cm}^2$ ,  $\sigma_4=4.5 \times 10^{-24} \text{ cm}^2$ ,  $F=350 \text{ mJ/cm}^2$ .

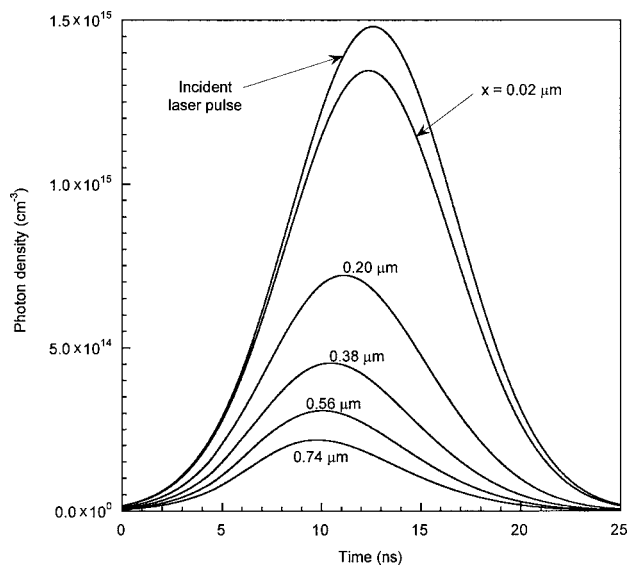


Fig. 7. Photon density temporal profiles predicted by the dynamic ablation model at five tissue depths. The temporal profile of the incident laser pulse is also shown. Dynamic model parameters:  $\Delta x=20 \text{ nm}$ ,  $P=0.8$ ,  $\sigma_3=4.5 \times 10^{-15} \text{ cm}^2$ ,  $\sigma_4=4.5 \times 10^{-24} \text{ cm}^2$ ,  $F=350 \text{ mJ/cm}^2$ .

depth. This behavior is expected because the tissue at any given depth is absorbing photons; hence a cumulative effect results that makes fewer photons available to underlying tissue. At a depth of only  $0.02 \mu\text{m}$ , the maximum photon density is already reduced by nearly 10% from that of the incident waveform. At  $0.74 \mu\text{m}$ , which is very close to the ablation depth of  $0.75 \mu\text{m}$  at this fluence, the maximum photon density is reduced by about 85% from that of the incident waveform. It is also interesting to

note that the peak photon density is shifted to sooner in the laser pulse with increasing tissue depth, an effect that is also attributed to the cumulative effect of the dynamic tissue absorption process, which increasingly truncates the trailing edge of the pulse waveform.

Figure 8 shows the absorption coefficient as a function of time for a fluence of  $350 \text{ mJ/cm}^2$  and at a fixed depth of  $0.74 \mu\text{m}$ , with the temporal profile of the photon density shown for reference. The absorption coefficient steadily increases, following the photon density and corresponding global reaction kinetics, up to the point where the ablation threshold is reached and ablation begins. At that instant in time, there is a sudden and marked reduction in the absorption coefficient due to the 10% volume expansion, as discussed above and implemented in the model. Note that ablation begins just prior to the temporal peak of the photon density, a characteristic that is the same at any location between the corneal surface and the ablation depth. Beyond this point, the absorption coefficient continues to increase, but at an increasingly slower rate, and then levels off at a maximum value of approximately  $22,650 \text{ cm}^{-1}$ . This value is consistent with the authors' previous work, in which it was suggested that a 25%–75% dynamic enhancement of the small-signal absorption coefficient value of  $16,000 \text{ cm}^{-1}$  is most probable under corneal ablative conditions.<sup>6</sup> The plateau behavior of the absorption coefficient is not due to any saturation effects or shortage of chromophores but rather to the steady decrease to zero in the photon density as the remainder of the laser pulse passes through. For the current model, the absorption coefficient will eventually approach its original (small-signal) value. However, this does not occur within the 25 ns laser pulse because of the slow kinetics for reaction II, which involves the recombination of the transient absorber (species 3) with water to form the stable nonabsorbing product (species 4). Regardless, the long-term behavior of the absorption coefficient ( $\sim 1 \mu\text{s}$  as time scale) for the ablated tissue is irrelevant, since this tissue is expelled from the corneal surface well before the arrival

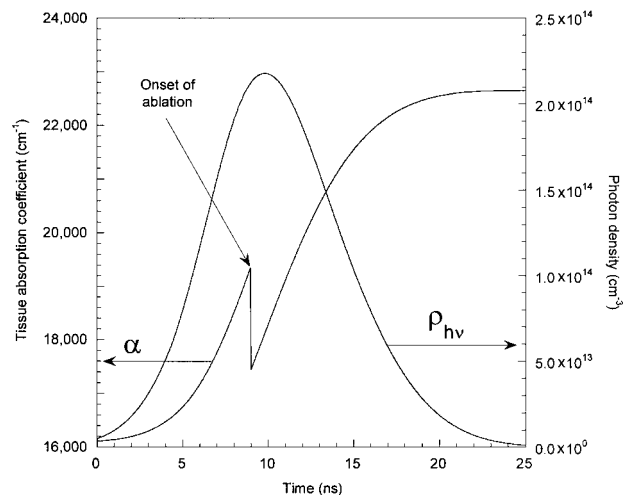


Fig. 8. Corneal tissue absorption coefficient as a function of time as predicted by the dynamic ablation model. The temporal profile of the incident laser pulse is also plotted using the secondary ordinate axis to the right. Both parameters are at a fixed depth of  $0.74 \mu\text{m}$ . Dynamic model parameters:  $\Delta x=20 \text{ nm}$ ,  $P=0.8$ ,  $\sigma_3=4.5 \times 10^{-15} \text{ cm}^2$ ,  $\sigma_4=4.5 \times 10^{-24} \text{ cm}^2$ ,  $F=350 \text{ mJ/cm}^2$ .

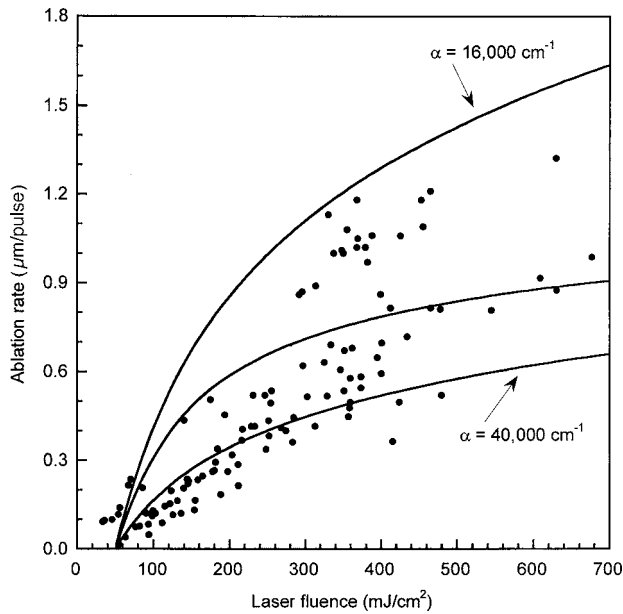


Fig. 9. Ablation rate as a function of laser fluence for ArF excimer laser ablation of corneal tissue, comparing reported experimental data<sup>8,48–55</sup> with values predicted by the dynamic ablation model (middle curve). Values predicted by the static Beer–Lambert law (upper and lower curves) are also included for absorption coefficients of 16,000 and 40,000  $\text{cm}^{-1}$ . Dynamic model parameters:  $\Delta x=20$  nm,  $P=0.8$ ,  $\sigma_3=4.5 \times 10^{-15}$   $\text{cm}^2$ ,  $\sigma_4=4.5 \times 10^{-24}$   $\text{cm}^2$ .

of the next laser pulse. Note that even at a laser repetition rate of 500 Hz (faster than current LASIK systems) the next laser pulse does not arrive for 2 ms, which corresponds to a significantly longer time scale than the temporal domain of the current dynamic model. Accordingly, the current model does not address the effect of the laser radiation on the underlying, unablated tissue or how this might affect the ablation process for subsequent laser pulses. Furthermore, previous work has shown that the ablation rate does not appear to change with the number of accumulated laser pulses.<sup>47</sup> This suggests that tissue just beneath the ablation zone is not significantly affected by the radiation over typical pulse-to-pulse separation times ( $\sim 10$  ms at 100 Hz repetition rate), thereby making the ablation process similar (i.e., independent) for all laser pulses. Future modeling efforts could address this issue by including a mechanism to explain the effect of subablative laser radiation on underlying corneal tissue.

Using the base conditions, the dynamic model was used to predict the ablation rate over a wide range of laser fluence spanning from just above the ablation threshold (50  $\text{mJ}/\text{cm}^2$ ) to 700  $\text{mJ}/\text{cm}^2$ . This is considered to cover the range of clinical refractive fluences, including Gaussian beam profiles, hence from about 250 to 600  $\text{mJ}/\text{cm}^2$ . Figure 9 shows the ablation rate plotted as a function of laser fluence, including results from the current dynamic model and a large body of corneal ablation rate data taken from a variety of published sources.<sup>8,48–55</sup> For comparison, also included in Fig. 9 are the results predicted by the static Beer–Lambert blow-off model using two different values for the absorption coefficient, namely, 16,000 and 40,000  $\text{cm}^{-1}$ . There are several important aspects of Fig. 9 to note. First, neither of the static Beer–

Lambert cases agrees well with the entire range of experimental data. Except at near-threshold fluence, the 16,000  $\text{cm}^{-1}$  case always overpredicts the ablation rate and never reaches a plateau. The 40,000  $\text{cm}^{-1}$  case is reasonably accurate at lower values of laser fluence, but it underpredicts most of the experimental data in the clinically relevant range of 300 to 600  $\text{mJ}/\text{cm}^2$ . The ablation rates predicted by the dynamic model fall between the two static Beer–Lambert cases. Specifically, at 350  $\text{mJ}/\text{cm}^2$ , the dynamic model predicts an ablation rate of 0.75  $\mu\text{m}/\text{pulse}$ , while the static Beer–Lambert law predicts a rate that is 60% higher (1.21  $\mu\text{m}/\text{pulse}$ ) for the 16,000  $\text{cm}^{-1}$  case and 40% lower (0.49  $\mu\text{m}/\text{pulse}$ ) for the 40,000  $\text{cm}^{-1}$  case. Although it is difficult to assess the true accuracy of the dynamic model owing to the large spread in the experimental data, the rate versus fluence curve predicted by the dynamic model for fluence values above 200  $\text{mJ}/\text{cm}^2$  passes directly through the middle of the data. To our knowledge, this is the first report of a dynamic photochemical model of the ArF excimer laser tissue ablation process that predicts ablation rates with reasonable accuracy over a relatively broad range of clinically relevant laser fluence values.

As discussed above, a significant factor in developing the current model is the implication of corneal tissue ablation rates on clinical refractive procedures. Previous work has shown that corneal tissue can dehydrate significantly within a short period of time.<sup>56</sup> In addition, corneal hydration is likely to differ between patients. Some prior studies have shown an increase in corneal tissue ablation rate with increasing hydration, while others have shown an opposite trend.<sup>57–59</sup> Therefore, it is considered important to investigate the relationship between ablation rate and corneal hydration predicted by the current dynamic model. Figure 10 presents the ablation rate as a function of corneal hydration, for a laser fluence of 350  $\text{mJ}/\text{cm}^2$

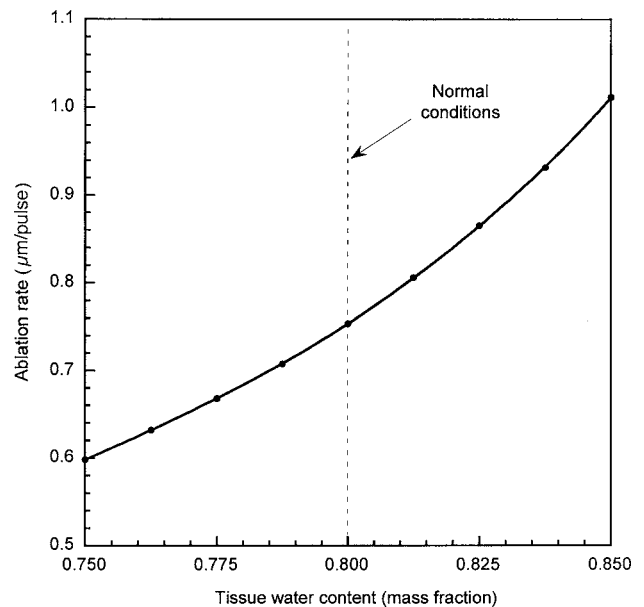


Fig. 10. Ablation rate as a function of corneal tissue water content, as predicted by the dynamic ablation model. Dynamic model parameters:  $\Delta x=20$  nm,  $\sigma_3=4.5 \times 10^{-15}$   $\text{cm}^2$ ,  $\sigma_4=4.5 \times 10^{-24}$   $\text{cm}^2$ ,  $F=350$   $\text{mJ}/\text{cm}^2$ .

and hydration fraction ( $P$ ) ranging from 0.75 to 0.85. Over this relatively small hydration range, the ablation rate increases from  $0.6 \mu\text{m}/\text{pulse}$  to over  $1.0 \mu\text{m}/\text{pulse}$ . The relationship is nonlinear, with the rate of increase in the ablation rate growing with increasing tissue hydration. This behavior follows directly from the proposed mechanism, in which increased hydration reduces the relative concentration of collagen, thereby slowing the kinetics of the formation of the transient absorber via Eq. (7) and thereby reducing the degree of dynamic absorptivity. Owing to inconsistencies in the literature and lack of definitive data, it is difficult to assess absolute behavior of the current model with regard to corneal hydration. Nevertheless, the dynamic model predicts a positive relationship between ablation rate and corneal hydration and furthermore predicts the ablation rate to be strongly influenced by relatively small changes in hydration, which certainly is of interest clinically.

#### 4. CONCLUSIONS

Detailed fluorescence measurements were conducted to determine the importance of laser-induced plasma formation and plasma shielding during the excimer laser tissue ablation through the clinically relevant fluence regime. The current conclusion, as based on careful spectroscopic measurements, is that plasma formation and plasma shielding are not important during corneal tissue ablation processes for the range of laser fluences examined in this study and relevant to clinical excimer laser refractive procedures.

Prior work has suggested that the ablation process is a dynamic photochemical phenomenon, a notion that is supported by the results of the corneal tissue fluorescence-emission experiments. In response, a dynamic model for excimer laser corneal tissue ablation was developed. The model is based on the differential form of the Beer-Lambert law but incorporates a dynamic absorption coefficient. The model is also capable of predicting the effect of varying tissue hydration on the ablation rate. As discussed above, the proposed ablation model is global and mechanistic and is therefore meant to capture the overall dynamic nature of the tissue ablation process rather than the fine details. Overall, the model was successful in providing reasonable agreement with a wide range of published corneal tissue ablation data, thereby providing a framework for further understanding the role of photochemical kinetics in ArF laser corneal tissue ablation.

#### ACKNOWLEDGMENTS

This work was supported in part by a grant from Alcon Research, Ltd.

Corresponding author David W. Hahn can be reached by e-mail at [dwhahn@ufl.edu](mailto:dwhahn@ufl.edu).

\*Current address, National Research Council Postdoctoral Research Associate Program, Naval Research Laboratory, Washington, D.C. 20375.

#### REFERENCES

1. G. Paltauf and P. E. Dyer, "Photochemical processes and effects in ablation," *Chem. Rev. (Washington, D.C.)* **103**, 487–518 (2003).
2. A. Vogel and V. Venugopalan, "Mechanisms of pulsed laser ablation of biological tissues," *Chem. Rev. (Washington, D.C.)* **103**, 577–644 (2003).
3. F. Manns, P. Milne, and J. M. Parel, "Ultraviolet corneal photoablation," *J. Refract. Surg.* **18**, 1–5 (2002).
4. G. H. Pettit and R. Sauerbrey, "Pulsed ultraviolet laser ablation," *Appl. Phys. A* **56**, 51–63 (1993).
5. J. V. McGrann, J. Neev, and M. W. Berns, "Physical characteristics of excimer laser-tissue interactions," in *Laser-Tissue Interaction III*, S. L. Jacques, ed., *Proc. SPIE* **1646**, 56–68 (1992).
6. B. T. Fisher and D. W. Hahn, "Measurement of small-signal absorption coefficient and absorption cross section of collagen for 193-nm excimer laser light and the role of collagen in tissue ablation," *Appl. Opt.* **43**, 5443–5451 (2004).
7. C. A. Puliafito, R. F. Steinert, T. F. Deutsch, F. Hillenkamp, E. J. Dehm, and C. M. Adler, "Excimer laser ablation of the cornea and lens: experimental studies," *Ophthalmology* **92**, 741–748 (1985).
8. C. A. Puliafito, K. Wong, and R. F. Steinert, "Quantitative and ultrastructural studies of excimer laser ablation of the cornea at 193 and 248 nanometers," *Lasers Surg. Med.* **7**, 155–159 (1987).
9. A. Lembares, X.-H. Hu, and G. W. Kalmus, "Absorption spectra of corneas in the far ultraviolet region," *Invest. Ophthalmol. Visual Sci.* **38**, 1283–1387 (1997).
10. Z. Bor, B. Hopp, B. Racz, G. Szabo, Z. Marton, I. Ratkay, J. Mohay, I. Suveges, and A. Fust, "Physical problems of excimer laser cornea ablation," *Opt. Eng.* **32**, 2481–2486 (1993).
11. G. H. Pettit and M. N. Ediger, "Corneal-tissue absorption coefficients for 193- and 213-nm ultraviolet radiation," *Appl. Opt.* **35**, 3386–3391 (1996).
12. A. D. Yablon, N. S. Nishioka, B. B. Mikic, and V. Venugopalan, "Measurement of tissue absorption coefficients by use of interferometric photothermal spectroscopy," *Appl. Opt.* **38**, 1259–1272 (1999).
13. V. N. Tokarev, J. G. Lunney, W. Marine, and M. Sentis, "Analytical thermal model of ultraviolet laser ablation with single-photon absorption in the plume," *J. Appl. Phys.* **78**, 1241–1246 (1995).
14. E. Sutcliffe and R. Srinivasan, "Dynamics of UV laser ablation of organic polymer surfaces," *J. Appl. Phys.* **60**, 3315–3322 (1986).
15. R. Srinivasan, B. Braren, D. E. Seeger, and R. W. Dreyfus, "Photochemical cleavage of a polymeric solid—details of the ultraviolet-laser ablation of poly(methyl methacrylate) at 193-nm and 248-nm," *Macromolecules* **19**, 916–921 (1986).
16. B. Lukyanchuk, N. Bityurin, S. Anisimov, N. Arnold, and D. Bauerle, "The role of excited species in ultraviolet-laser materials ablation. 3. Non-stationary ablation of organic polymers," *Appl. Phys. A* **62**, 397–401 (1996).
17. J. R. Jimenez, R. G. Anera, and L. J. del Barco, "Equation for corneal asphericity after corneal refractive surgery," *J. Refract. Surg.* **19**, 65–69 (2003).
18. R. G. Anera, J. R. Jimenez, L. J. del Barco, and E. Hita, "Changes in corneal asphericity after laser refractive surgery, including reflection losses and nonnormal incidence upon the anterior cornea," *Opt. Lett.* **28**, 417–419 (2003).
19. J. R. Jimenez, R. G. Anera, L. J. del Barco, and E. Hita, "Influence of laser polarization on ocular refractive parameters after refractive surgery," *Opt. Lett.* **29**, 962–964 (2004).
20. J. R. Jimenez, R. G. Anera, J. A. Diaz, and F. Perez-Ocon, "Corneal asphericity after refractive surgery when the Munnerlyn formula is applied," *J. Opt. Soc. Am. A* **21**, 98–103 (2004).
21. J. R. Jimenez, R. G. Anera, L. J. del Barco, E. Hita, and F. Perez-Ocon, "Correction factor for ablation algorithms used

- in corneal refractive surgery with gaussian-profile beams," *Opt. Express* **13**, 336–343 (2005).
22. J. R. Jimenez, F. Rodriguez-Matin, R. G. Anera, and L. J. del Barco, "Deviations of Lambert–Beer's law affect corneal refractive parameters after refractive surgery," *Opt. Express* **14**, 5411–5417 (2006).
  23. T. P. Hughes, *Plasmas and Laser Light* (Wiley, 1975).
  24. Y. B. Zel'dovich and Y. P. Raizer, *Physics of Shock Waves and High-Temperature Hydrodynamic Phenomena* (Dover, 2002).
  25. G. Bekefi, *Principles of Laser Plasmas* (Wiley, 1976).
  26. J. F. Ready, *Effects of High-Power Laser Radiation* (Academic, 1971).
  27. I. G. Pallikaris, H. S. Gini, G. A. Kounis, D. Anglos, T. G. Papazoglou, and L. P. Naoumidis, "Corneal hydration monitored by laser-induced breakdown spectroscopy," *J. Refract. Surg.* **14**, 655–660 (1998).
  28. L. J. Radziemski and D. A. Cremers, eds., *Laser-Induced Plasmas and Applications* (Marcel Dekker, 1989).
  29. V. Hohreiter, J. E. Carranza, and D. W. Hahn, "Temporal analysis of laser-induced plasma properties as related to laser-induced breakdown spectroscopy," *Spectrochim. Acta, Part B* **59**, 327–333 (2004).
  30. C. G. Parigger, D. H. Plemmons, and E. Oks, "Balmer series  $H_{\beta}$  measurements in a laser-induced hydrogen plasma," *Appl. Opt.* **42**, 5992–6000 (2003).
  31. E. Oks, "A new spectroscopic effect resulting in a narrowing of hydrogen lines in dense plasmas," *J. Quant. Spectrosc. Radiat. Transf.* **65**, 405–414 (2000).
  32. J. D. Bradshaw, M. O. Rodgers, and D. D. Davis, "Single photon laser-induced fluorescence detection of NO and SO<sub>2</sub> for atmospheric conditions of composition and pressure," *Appl. Opt.* **21**, 2493–2500 (1982).
  33. J. B. Simeonsson and R. C. Sausa, "A critical review of laser photofragmentation-fragment detection techniques for gas phase chemical analysis," *Appl. Spectrosc. Rev.* **31**, 1–72 (1996).
  34. M. H. Nunez, P. Cavalli, G. Petrucci, and N. Omenetto, "Analysis of sulfuric acid aerosols by laser-induced breakdown spectroscopy and laser-induced photofragmentation," *Appl. Spectrosc.* **54**, 1805–1816 (2000).
  35. M. H. Nunez and N. Omenetto, "Experimental investigation of sodium emission following laser photofragmentation of different sodium-containing aerosols," *Appl. Spectrosc.* **55**, 809–815 (2001).
  36. P. N. Prasad, *Introduction to Biophotonics* (Wiley, 2003).
  37. M. N. Ediger, G. H. Pettit, R. P. Weiblinger, and C. H. Chen, "Transmission of corneal collagen during ArF excimer laser ablation," *Lasers Surg. Med.* **13**, 204–210 (1993).
  38. M. N. Ediger, G. H. Pettit, and R. P. Weiblinger, "Noninvasive monitoring of excimer laser ablation by time-resolved reflectometry," *Refract. Corneal Surg.* **9**, 268–275 (1993).
  39. G. H. Pettit and M. N. Ediger, "Pump/probe transmission measurements of corneal tissue during excimer laser ablation," *Lasers Surg. Med.* **13**, 363–367 (1993).
  40. G. H. Pettit, M. N. Ediger, and R. P. Weiblinger, "Dynamic optical properties of collagen-based tissue during ArF excimer laser ablation," *Appl. Opt.* **32**, 488–493 (1993).
  41. M. N. Ediger, G. H. Pettit, and D. W. Hahn, "Enhanced ArF laser absorption in a collagen target under ablative conditions," *Lasers Surg. Med.* **15**, 107–111 (1994).
  42. G. H. Pettit, M. N. Ediger, and R. P. Weiblinger, "Excimer laser ablation of the cornea," *Opt. Eng.* **34**, 661–667 (1995).
  43. P. Simon, "Time-resolved ablation site photography of XeCl-laser irradiated polyimide," *Appl. Phys. B* **48**, 253–256 (1989).
  44. S. Lerman, *Radiant Energy and the Eye* (Macmillan, 1980).
  45. S. R. Turns, *An Introduction to Combustion: Concepts and Applications* (McGraw-Hill, 2000).
  46. P. Anfinrud, R. de Vivie-Riedle, and V. Engel, "Ultrafast detection and control of molecular dynamics," *Proc. Natl. Acad. Sci. U.S.A.* **96**, 8328–8329 (1999).
  47. B. T. Fisher and D. W. Hahn, "Determination of excimer laser ablation rates of corneal tissue using wax impressions of ablation craters and white-light interferometry," *Ophthalmic Surg. Lasers Imaging* **35**, 41–51 (2004).
  48. D. S. Aron-Rosa, J. L. Boulnoy, F. Carre, J. Delacour, M. Gross, M. LaCour, J. C. Olivo, and J. C. Timsit, "Excimer laser surgery of the cornea: qualitative and quantitative aspects of photoablation according to the energy density," *J. Cataract Refractive Surg.* **12**, 27–33 (1986).
  49. M. W. Berns, L. Chao, A. W. Giebel, L. H. Liaw, J. Andrews, and B. VerSteege, "Human corneal ablation threshold using the 193-nm ArF excimer laser," *Invest. Ophthalmol. Visual Sci.* **40**, 826–830 (1999).
  50. M. Campos, X. W. Wang, L. Hertzog, M. Lee, T. Clapham, S. L. Trokel, and P. J. McDonnell, "Ablation rates and surface ultrastructure of 193 nm excimer laser keratectomies," *Invest. Ophthalmol. Visual Sci.* **34**, 2493–2500 (1993).
  51. F. E. Fantes and G. O. Waring, "Effect of excimer laser radiant exposure on uniformity of ablated corneal surface," *Lasers Surg. Med.* **9**, 533–542 (1989).
  52. H. J. Huebscher, U. Genth, and T. Seiler, "Determination of excimer laser ablation rate of the human cornea using *in vivo* Scheimpflug videography," *Invest. Ophthalmol. Visual Sci.* **37**, 42–46 (1996).
  53. M. S. Kitai, V. L. Popkov, V. A. Semchishen, and A. A. Kharizov, "The physics of UV laser cornea ablation," *IEEE J. Quantum Electron.* **27**, 302–307 (1991).
  54. R. R. Krueger and S. L. Trokel, "Quantitation of corneal ablation by ultraviolet laser light," *Arch. Ophthalmol. (Chicago)* **103**, 1741–1742 (1985).
  55. P. P. Van Saarloos and I. J. Constable, "Bovine corneal stroma ablation rate with 193-nm excimer laser radiation: quantitative measurement," *Refract. Corneal Surg.* **6**, 424–429 (1990).
  56. B. T. Fisher, K. A. Masiello, M. H. Goldstein, and D. W. Hahn, "Assessment of transient changes in corneal hydration using confocal Raman spectroscopy," *Cornea* **22**, 363–370 (2003).
  57. P. J. Dougherty, K. L. Wellish, and R. K. Maloney, "Excimer laser ablation rate and corneal hydration," *Am. J. Ophthalmol.* **118**, 169–176 (1994).
  58. G. O. Waring, "Development of a system for excimer laser corneal surgery," *Trans. Am. Ophthalmol. Soc.* **87**, 854–983 (1989).
  59. M. H. Feltham, M. Optom, and F. Stapleton, "The effect of water content on the 193 nm excimer laser ablation," *Clin. Exp. Ophthalmol.* **30**, 99–103 (2002).